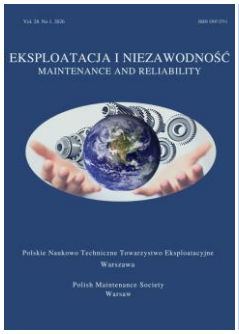

Eksploatacja i Niezawodnosc – Maintenance and Reliability

Volume 28 (2026), Issue 1

journal homepage: http://www.ein.org.pl

Article citation info:
Xie J, Meng L, Parametric Fault Diagnosis Approach for the Power Switching Device of Three-Phase Inverter Utilizing HTISFF-VSPWN, Eksploatacja i Niezawodnosc – Maintenance and Reliability 2026: 28(1) http://doi.org/10.17531/ein/209902

Parametric Fault Diagnosis Approach for the Power Switching Device of Three-Phase Inverter Utilizing HTISFF-VSPWN

Indexed by: Web of Science Group

Jinyang Xie[a], Linghui Meng[b,*]

[a] [1]School of Electrical Engineering, Beijing Jiaotong university, China
[2]Science and Technology on Reliability Physics and Application of Electronic Component Laboratory, China Electronic Product Reliability and Environmental Testing Research Institute Guangzhou, China

Highlights

- Hilbert transform is used for feature extraction and data dimensionality reduction.
- Multi-scale feature extraction is realized by constructing variable step size volume block.
- Highlight important features through reverse attention mechanism.
- Multiple source features are fused as the final feature tensor.

Abstract

The three-phase inverter plays a pivotal role in various fields such as modern industry, rail transit, and aerospace. However, early parametric fault diagnosis of inverter switching devices faces challenges due to redundant feature data and the subtle differences in fault features across different degradation levels. To overcome these issues, we propose a novel method called HTISFF-VSPWN for parametric fault diagnosis. Our approach involves extracting key characteristics from the three-phase voltage and current data of the inverter using the Hilbert transform. Following this, we train the model after dimension reduction. Experimental results conducted on SIC MOSFETs parametric fault data reveal that HTISFF-VSPWN outperforms other methods. Compared to 1DCNN, 1DCNN-LSTM, DRSN, IWOA-1DCNN-LSTM and MTF-SPCNN, our method achieves a diagnostic accuracy improvement of 3.69%, 2.81%, 1.6%, 0.67% and 0.92% respectively. The diagnostic time was reduced by 64s, 106s, 120s, 182s and 99s compared with the comparison method.

Keywords
feature dimension reduction, feature extraction, parametric fault, three-phase inverter

This is an open access article under the CC BY license (https://creativecommons.org/licenses/by/4.0/)

1. Introduction

Three-phase inverters are integral in modern industries, converting DC power to AC voltage with variable frequency and amplitude 1. Power semiconductor devices like insulated-gate bipolar transistors (IGBTs) and metal-oxide-semiconductor field-effect transistors (MOSFETs) serve as primary switches in these inverters 23. Ensuring their stable operation is crucial for the inverters' proper functioning. Statistics indicate that approximately 38% of faults in power equipment are attributable to these switching devices 4.

Faults in power switching devices primarily fall into two categories: Structural Hard Failures (SHF) and Parametric Soft Failures (PSF) 5. SHF typically manifests as Short Circuit Faults (SCF) and Open Circuit Faults (OCF) 6. SCF leads to rapid increases in voltage and current over a short period, while OCF can be detected by circuit breakers and converted to an open circuit state. Therefore, research on fault diagnosis methods for OCF holds greater significance than for SCF.

Diagnostic methods for OCF generally fall into two types:

(*) Corresponding author.
E-mail addresses: J. Xie, (ORCID: 0009-0005-5507-6525) xjy19980920@163.com, L. Meng (ORCID:0000-0001-5915-4395) menglinghui@ceprei.com,

model-based and data-driven methods. Model-based approaches require understanding the dynamic characteristics and operational mechanisms of the system to establish accurate mathematical models. Residual signals are then analyzed based on input and output signal detections for fault diagnosis 7. However, these methods heavily rely on system model accuracy and are susceptible to parameter variations, which may result in lower fault diagnosis accuracy. In contrast, data-driven intelligent diagnosis methods aim to extract fault features from extensive historical data. These methods employ intelligent diagnostic techniques to establish mappings between fault features and fault modes without relying on precise system models, thereby enhancing diagnostic accuracy 8. For instance, Q.Y. Wang et al. proposed an open circuit fault diagnosis method for inverters using mean value voltage combined with Extreme Learning Machines (ELM). Their approach focuses on analyzing fault characteristics related to OCF in traction inverters, utilizing mean voltage signals for rapid fault detection. Subsequently, fault feature vectors are extracted from stator currents and an offline-trained ELM model is employed for online diagnostic testing, achieving effective fault diagnosis 9, However, when the external environmental noise is significant, the ELM exhibits a diminished capacity to extract fault features from the current, leading to reduced robustness of the model in such scenarios. Similarly, Q. Sun et al. developed a Hybrid Convolutional Neural Network (HCNN) model comprising one-dimensional (1D-CNN) and two-dimensional (2D-CNN) convolutional neural networks. They utilized preprocessed three-phase current signal spectra as input data for HCNN model training. Their approach culminates in the realization of OCF diagnosis in inverters through fully connected layers, demonstrating robust diagnostic capabilities 10, the implementation of a hybrid model exacerbates the extraction of redundant features to some extent, thereby hindering the model's ability to perform efficient fault diagnosis. B.Y. Song et al. [11] proposed to optimize the hyperparameters of bidirectional LSTM by particle swarm optimization algorithm, aiming to achieve accurate diagnosis in the case of limited samples, but there were problems of low diagnostic efficiency and unclear performance of the model in parametric fault diagnosis.

In fact, the diagnosis of SHF primarily serves as a corrective action post-incident. By accurately identifying the fault type and location, the impact on the safe and stable operation of the power system, once the fault has occurred, can be substantial 12. Typically, SHF is preceded by PSF. Real-time monitoring and defect diagnosis of switch tube health based on PSF can forecast SHF risks in advance, enabling preemptive isolation measures to prevent actual faults 13. I. Bandyopadhyay et al. 14 conducted feature extraction through time-domain computation and utilized a support vector machine classifier to identify early faults based on motor current characteristics. This method achieves accurate early fault diagnosis but does not assess fault severity. Y.Y. Jiang et al. 15 employed Variational Mode Decomposition (VMD) to decompose parameters into multiple components, applying wavelet transform (WT) to extract wavelet energies from each mode component for fault feature extraction and dimensionality reduction. Despite achieving high diagnostic accuracy using CNN, this approach does not address noise interference in the diagnostic model. Z.Y. Li et al. 16 proposed an inverter switch tube health diagnosis method combining Gram Angle Field (GAF) with a parallel CNN. Voltage and current signals from the inverter output are converted into 2D feature images using GAF, albeit with potential feature loss during image conversion. Y.B. Cui et al. [17] utilized the Gram angular compound field to map the inverter voltage signal, thereby generating a two-dimensional feature image that was subsequently processed using AlexNet for feature extraction. The final diagnostic result was produced by the Softmax layer. While these methods effectively leverage the feature extraction capabilities of two-dimensional diagnostic models, they overlook the issue of feature loss during image conversion, particularly in noisy environments where fault information can be obscured by noise, leading to diminished model robustness.

Furthermore, data-driven diagnostic models are highly reliant on the effectiveness of training data, leading existing models to often utilize the characteristic data of diagnostic subjects directly for model training. This approach neglects the significance of dimensionality reduction, resulting in redundant training data that complicates model training and prolongs diagnosis time. Additionally, the inherent structure of the model significantly influences diagnostic efficiency; repeated extraction of similar information can lead to increased feature

extraction times when dealing with large datasets.

This paper proposed a PSF diagnosis model for inverters based on Hilbert transform interval sampling feature fusion (HTISFF) and variable step size parameter weighting network (VSPWN), aiming to achieve accurate diagnosis while considering the influence of noise on the diagnostic model. The model extracts instantaneous frequency and amplitude features from the three-phase voltage and current signals at the output of the inverter by using HT. These extracted features are fused after interval sampling and utilized as input features for the diagnostic model.

The VSPWN is constructed with a variable step size weighting module and a reverse attention mechanism, which effectively extracts features of different scales from the input features. Finally, the PSF diagnosis of the three-phase inverter is realized through a fully connected layer.

The main contributions of this paper can be summarized as follows:

1) The HT is employed to extract features from the voltage and current signals from three-phase inverter individually. The extracted features are then sampled at intervals according to the data acquisition frequency to reduce the data scale. Ultimately, the voltage and current features, post-interval sampling, are concatenated to serve as the input for the diagnostic model;
2) A two-layer convolutional approach is utilized to construct variable step-size blocks (where the convolutional kernel sizes and strides of the dual-layer convolution are mismatched), enabling multi-scale feature extraction. Important features post the variable step-size blocks are then highlighted through the reverse attention mechanism. The highlighted feature data is weighted as the output of the variable step-size weighting module to enhance the diagnostic accuracy of the model.

The specific flow of PSF diagnosis model for three-phase inverter power switching device is shown in Fig 1.

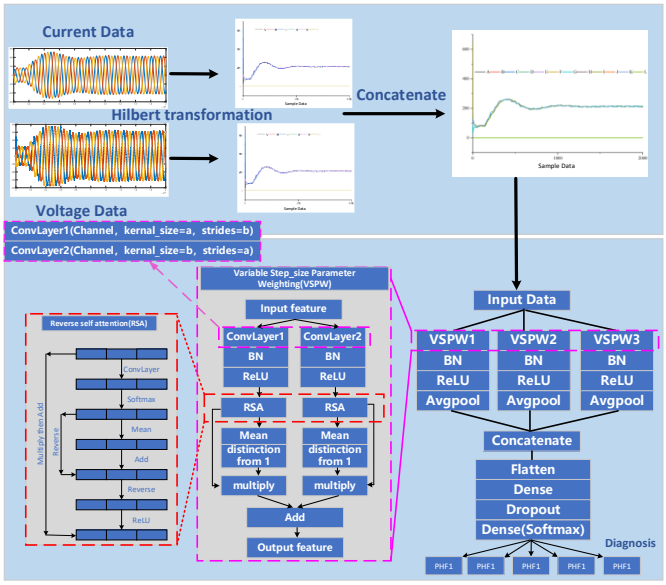

Fig. 1. PSF diagnostic flow chart of three-phase inverter power switch device

2. Proposed Method

Due to minimal differences in PSF of voltage and current signals among various degrees of three-phase inverters, effectively extracting features for the diagnostic model poses challenges. To utilize fault features effectively, it is crucial to ensure feature distinctiveness while reducing data volume. We proposed using HT to extract instantaneous frequency and amplitude features from the original three-phase voltage and current signals, followed by interval sampling based on the data acquisition frequency. After sampling, the voltage and current characteristics are segmented as input features for the diagnostic model VSPWN.

A. Hilbert transform interval sampling feature fusion

1) Hilbert transform

The frequency of non-stationary signals varies over time, and traditional time-frequency analysis techniques can only capture the overall characteristics of the signal within a window, lacking the ability to depict instantaneous signal characteristics at specific moments. Instantaneous frequency provides detailed local signal characteristics at each moment, varying with time and obtainable through HT of the signal.

a) Perform a HT on the signal $\mu(t)$:

$$\hat{\mu}(t) = \frac{1}{\pi}\int_{-\infty}^{\infty}\frac{\mu(\tau)}{t-\tau}d\tau = \mu(t) * \frac{1}{\pi t} \tag{1}$$

Therefore, it can be inferred that the HT transformation of the signal is equivalent to the output of the signal through a

linear system with an impulse response $\frac{1}{\pi t}$, accurately representing the instantaneous characteristics of the signal. Following HT transformation, the amplitude of each frequency component remains unchanged, while the phase shifts by 90°.

b) Construction the analytic signal of $\mu(t)$:

$$z(t) = \mu(t) + j\hat{\mu}(t) = a(t)e^{j\theta(t)} \quad (2)$$

$a(t)$ and $\theta(t)$ are the instantaneous amplitude and instantaneous phase of the analytic signal:

$$a(t) = \sqrt{\mu^2(t) + \hat{\mu}^2(t)} \quad (3)$$

$$\theta(t) = \arctan\left(\frac{\hat{\mu}(t)}{\mu(t)}\right) \quad (4)$$

Through instantaneous phase, the instantaneous angular frequency ω(t) of the signal can be obtained:

$$\omega(t) = \frac{d\theta(t)}{dt} \quad (5)$$

c) Therefore, the instantaneous frequency can be obtained from formula 1.

$$v(t) = \frac{1}{2\pi}\omega(t) = \frac{1}{2\pi}\frac{d\theta(t)}{dt} \quad (6)$$

Since the voltage and current data of three-phase inverters can express the device state through the amplitude and frequency of the waveform, the extraction of the instantaneous frequency and instantaneous amplitude of the above data through HT is conducive to magnify the state changes of three-phase inverters caused by device parametric faults.

2) **Feature data interval sampling**

After applying HT, the characteristic data of the three-phase voltage and current from the three-phase inverter expanded from the original 3 columns to 6 columns. This increase in data volume raises the complexity of training the diagnostic model. Therefore, we reduced the dataset scale through interval sampling, as detailed in Fig 2. The reduced voltage and current feature data are concatenated along dimension 1. Specifically, the A-phase current data is sampled at intervals post-HT, resulting in retention of 8000 data points.

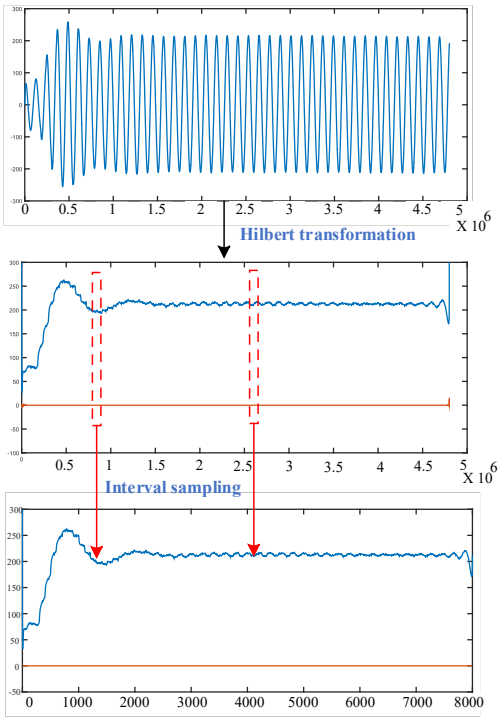

Fig. 2. Schematic diagram of current data interval sampling

B. Variable Step_size Parameter Weighting Network (VSPWN)

1) **Reverse Self-Attention (RSA)**

The differences in features among PSFs with varying degrees are minimal, posing challenges for the diagnostic model to effectively extract distinguishing characteristics. This limitation hinders the model's ability to accurately identify PSFs across different levels. To address this issue and enhance the effective extraction of subtle distinctions between PSFs, we propose a feature enhancement method: RSA (Relevance-Sensitive Attention) can facilitate feature extraction by deliberately emphasizing significant attributes while diminishing less critical ones within the feature data. The specific process is illustrated in Figure 3. Following the application of RSA on the feature data from three-phase inverters, the significance of points indicative of device state changes will be amplified, thereby enabling more precise extraction of these distinct features by the model.

For the input tensor $\boldsymbol{x} = [x_1 \quad x_2 \quad \cdots \quad x_n]$, Firstly, the proportion weight S_{x_i} is obtained from the input tensor by the Softmax function,

$$S_{x_i} = \frac{e^{x_i}}{\sum_{j=1}^{n} e^{x_j}} \quad (7)$$

Then calculate the mean $M_{S_{x_i}}$ for S_{x_i}:

$$M_{S_{x_i}} = \frac{\sum_{i=1}^{n} S_{x_i}}{n} \tag{8}$$

Pruning the original input tensor after reversal by $M_{S_{x_i}}$:

$$-x_i + M_{S_{x_i}} \tag{9}$$

The tensors after pruning are reversed again, and then positive filtering is performed on the reversed tensors through ReLU, and then key features of the original tensors are highlighted through the filtered tensors:

$$max\left[x_i - M_{S_{x_i}}, \quad 0\right] + x_i \tag{10}$$

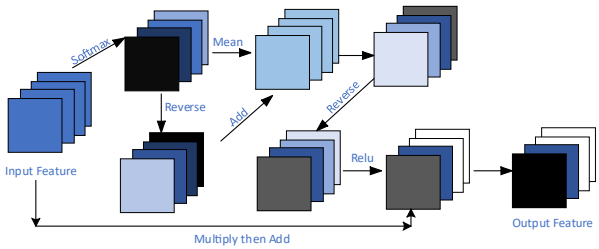

Fig. 3. Flowchart of RSA

2) **Variable Step Size Parameter weighting module (VSPWM)**

The feature extraction process of the convolutional layer can be summarized as follows: data is intercepted using a frame of specified convolution kernel size to extract features with a specified stride. However, the features extracted vary with different convolutional kernel sizes and stride lengths.

The convolution layer is mainly composed of several convolution kernels with local perception and parameter sharing characteristics. By performing convolution operations to extract the features of input data, multiple features can be learned and the computation parameters and computation amount can be reduced.

$$z_j^l = \sum_{i=1}^{n} k_{ij}^l * a_i^{l-1} + b_j^l \tag{11}$$

z_j^l is the output feature vector after the j convolution operation of layer l; k_{ij}^l is the j-th convolution kernel on the i channel of layer l; a_i^{l-1} is the i input feature vector of layer l; b_j^l is the offset item, used to adjust the offset of the output of the convolution operation;$*$ is the convolution operation.

In the convolutional layer, the kernel size and strides collectively influence the dimensions of the output tensor from the convolutional layer.

$$output_{size} = \left(\frac{input_{size} - kernal_{size}}{strides}\right) + 1 \tag{12}$$

After the convolution operation, the activation function is used to realize the nonlinear transformation of each convolution output vector. At present, the activation function commonly used in convolutional neural networks is ReLU function, which has the advantages of high computational efficiency and fast convergence speed, and is defined as:

$$c_j^l(p) = max\{0, \quad z_j^l(p)\} \tag{13}$$

Where $c_j^l(p)$ is the output and p is the p-th element in the output eigenvector after the convolution operation. And the batch normalization layer can reduce the risk of overfitting during model training by following steps:

1) Calculate the mean of each dimension

$$\mu_\beta = \frac{1}{m}\sum_{i=1}^{m} x_i \tag{14}$$

μ_β is the dimensional average.

2) Calculate the variance of each dimension

$$\sigma_\beta^2 = \frac{1}{m}\sum_{i=1}^{m}\left(x_i - \mu_\beta\right)^2 \tag{15}$$

σ_β^2 is the dimensional variance.

3) Each dimension of data is normalized

$$\hat{x}_i = \frac{x_i - \mu_\beta}{\sqrt{\sigma_\beta^2 + \varepsilon}} \tag{16}$$

$\hat{x}_i$ is the normalized processing value; ε is the value of the initialization parameter.

Sometimes, a large stride can lead to feature loss, while a small stride may cause redundant feature extraction, resulting in information redundancy. In this paper, we proposed a multi-scale feature extraction method that achieves multi-scale extraction of feature data by coordinating a small convolution kernel with a long volume layer and a large convolution kernel with a small volume layer, also utilizing a long volume layer. Furthermore, we implemented the mentioned operation through two branches, with the following distinction: the parameters of convolution layer 1 in branch 1 and convolution layer 2 in branch 2 correspond to each other; similarly, the parameters of convolution layer 2 in branch 1 and convolution layer 1 in branch 2 correspond to each other, thus avoiding feature loss due to excessive movement of the convolution kernel. Fig. 4. describes the operation of the two different convolution kernel_size and step collocation methods. The models have

different receptive fields through different convolution kernel move steps, and different convolution kernel sizes make each convolution focus on different features. The combination of the two enables the models to achieve effective feature extraction while having multiple receptive fields.

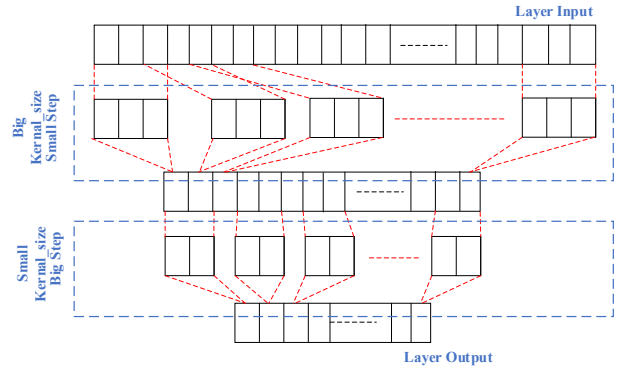

(a)

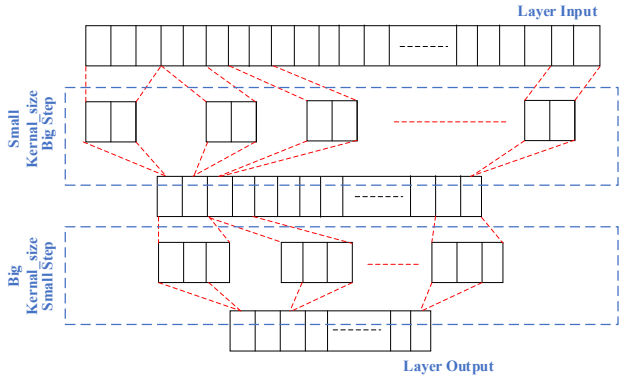

(b)

Fig. 4. Different Kernal_size and step collocation diagram

The feature data extracted from both branches are combined using RSA and serve as the output feature of VSPWM. Its operational diagram is illustrated in Fig. 5. In subsequent usage, we will use (a, b) to describe the parameters of the VSPWM utilized, indicating that the convolution kernel size of branch 1 is a, the step size of branch 2 is b, and the step size of branch 2 is a.

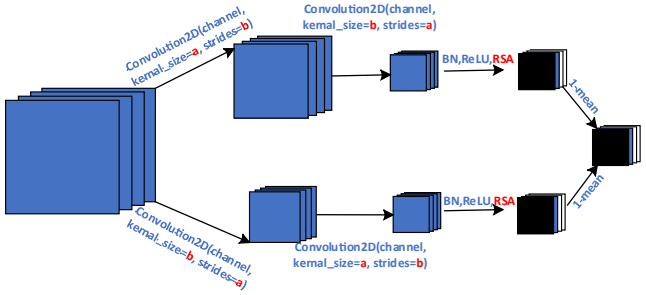

Fig. 5. VSPWM flow diagram

C. Variable step size parameter weighting network

The overall architecture of VSPWN is depicted in Fig. 6. Following HTISFF, the three-phase voltage and current signals from the inverter are utilized as input features for VSPWN. Subsequently, VSPWN conducts multi-scale feature extraction and feature enhancement using three sets of distinct parameters. The features are then concatenated through normalization, activation, and average pooling layers. The concatenated feature data is flattened directly via a flattening layer, enabling PSF diagnosis of the three-phase inverter through fully connected and dropout layers.

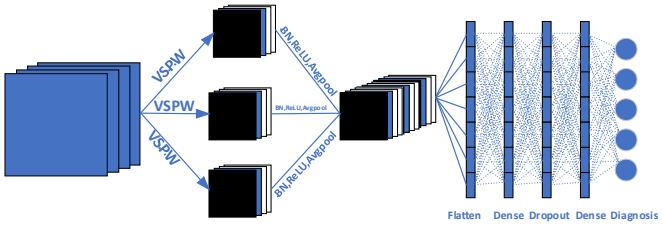

Fig. 6. Overall architecture of VSPWN

3. PSF Data Generation Of Three-Phase Inverter

The common inverter system structure is shown in Fig. 7, which is generally composed of four parts: DC side, inverter bridge, LC filter circuit and load.

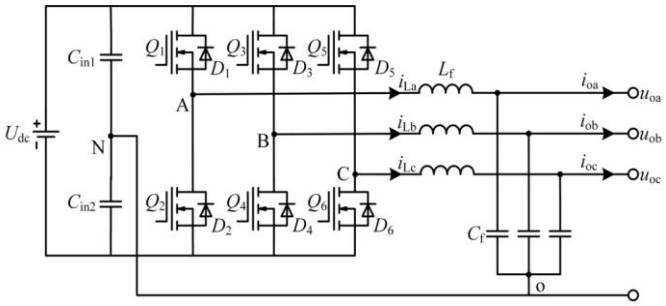

Fig. 7. Inverter system topology

Due to advancements in power electronic devices, the proportion of nonlinear loads in electrical systems is increasing. As significant sources of harmonics, these loads introduce substantial harmonic currents, resulting in harmonic distortion of the output voltage. Given the periodic nature of these harmonics, which are multiples of the fundamental wave, repetitive control emerges as a viable strategy for system control.

This paper focuses on a three-phase inverter utilizing SIC MOSFETs as power switching devices. It establishes a simulation platform in Simulink, employing S-Function to simulate both discrete and continuous systems. Fig. 8. illustrates

the construction of the inverter simulation system in Simulink. To leverage the benefits of SiC devices fully, the system's switching frequency is set to 30 kHz, with a control frequency of 60 kHz. This higher switching frequency allows the cutoff frequency of the LC filter circuit to be raised to 3 kHz, significantly reducing the volume of passive components in the system and enhancing its power density.

The LC circuit parameters are designed to minimize the volume of passive devices: the filter inductance L = 0.0773 mH and the filter capacitance C = 36.5 μF. The system is rated at 100 kVA.

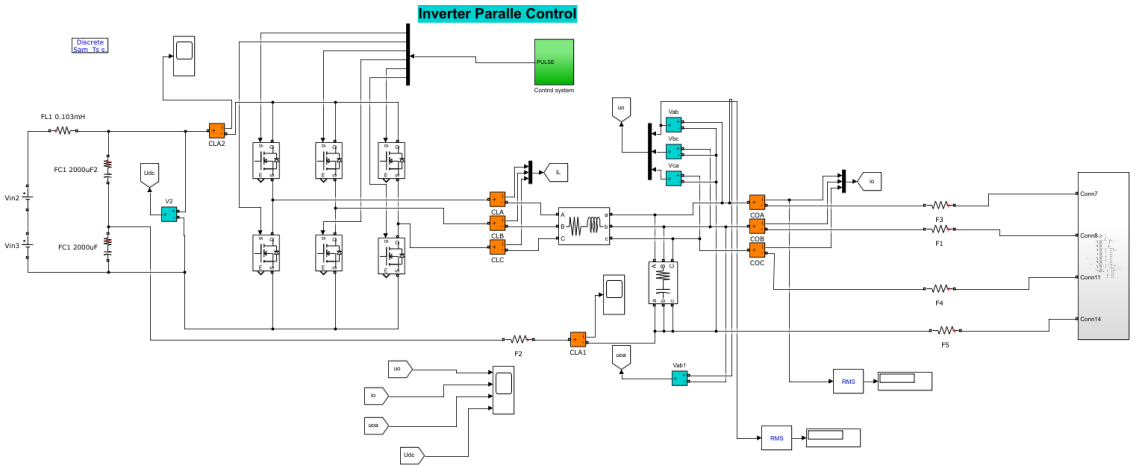

Fig. 8. Overall simulation model of inverter.

Based on the mentioned three-phase inverter simulation model focusing on SIC MOSFETs, this study explores a PSF diagnosis model for power switching devices in three-phase inverters. By individually varying the MOSFET's on-resistance, we simulate various degrees of parametric faults, using Q1 in Fig 6 as an example. The on-resistance is set to a healthy state (7.5 mΩ) and different levels of PSF (10 mΩ, 50 mΩ, 75 mΩ, 90 mΩ).

Table 1 presents a comparison of modulated waveforms for phases A and B under different on-resistances. This comparison aims to clearly delineate differences in third harmonic amplitudes, total harmonic distortion (THD), and other waveform parameters across phases under varying on-resistances.

Table 1. Comparison table of A and B phase modulated waves with different on-resistors

On-resistance /mΩ	Voltage amplitude of A phase modulated wave/THD/ third harmonic amplitude	Voltage amplitude of B phase modulated wave/THD/ third harmonic amplitude
7.5	338.4V/2.52%/6.467V	338.2V/2.66%/6.673V
10	338.4V/2.52%/6.028V	337.5V/2.57%/6.162V
50	341.9V/2.52%/6.076V	338.2V/2.67%/6.693V
75	344.2V/2.51%/6.008V	337.2V/2.57%/6.172V
90	345.4V/2.49%/5.919V	337.1V/2.57%/6.190V

4. Model Structure Comparison Experiment

To construct the most suitable model for PSF diagnosis of three-phase inverters, comparative experiments were conducted using different structures of VSPWN. These experiments involved high-temporal-resolution sampling of original three-phase voltage and current data, resulting in three types of sampled data: 2000, 4000, and 8000 data points, to investigate the impact of different data sizes on the diagnostic capability of the model post-sampling. Additionally, the effects of input model data types were compared, including the use of only three-phase voltage data, only three-phase current data, and both voltage and current data.

When the fault data was used as input to the diagnostic model, the number of VSPWM within VSPWN was varied to study the influence of different VSPWM quantities on the model's performance. The specific diagnostic outcomes are illustrated in Fig. 9. to Fig. 15. During model training, data was segmented through overlapping sampling; each sample

contained 1000 data points, with a moving step size of 10. The VSPWM model featured 64 convolutional kernels, with a batch size of 4. The optimizer utilized was Adam, with a learning rate of 0.0001, and the loss function employed was Cross Entropy.

Fig. 9. to Fig. 11. depict the utilization of VSPWM within VSPWN, where parameters (3,5), (4,6), and (5,7) are respectively applied. In these figures, 'C2000' denotes the use of original three-phase current data from the inverter, subjected to interval sampling post-HT processing. 'V2000' indicates the use of three-phase voltage data as the original feature set, while 'VC2000' employs both three-phase voltage and current data. For 'VC2000', interval sampling via HITS is conducted, retaining 2000 sampled points for each feature data, which are subsequently concatenated and fed into the diagnostic model.

	C2000	C4000	C8000	V2000	V4000	V8000	VC2000	VC4000	VC8000
Final Accuracy	0.9693	1	0.9975	0.6807	0.9956	0.2517	1	1	0.9979
Std	0.0898	0.0349	0.0276	0.1162	0.0352	0.1059	0.0675	0.0578	0.0169
Upper confidence limit	0.7552	0.8877	0.8926	0.4448	0.8986	0.6367	0.8371	0.8443	0.9351
Lower confidence limit	0.8747	0.9622	0.9589	0.5809	0.9736	0.7665	0.9408	0.8402	0.987
Mean	0.815	0.9249	0.9257	0.5128	0.9361	0.7016	0.8889	0.8923	0.961

Fig. 9. Diagnosis results of VSPWM(3,5)

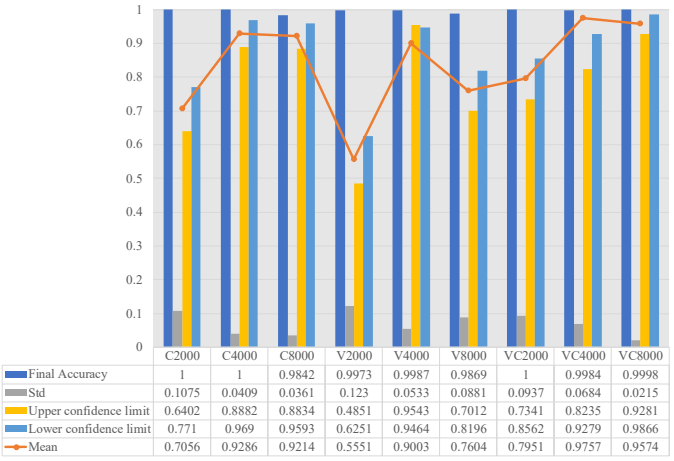

	C2000	C4000	C8000	V2000	V4000	V8000	VC2000	VC4000	VC8000
Final Accuracy	1	1	0.9842	0.9973	0.9987	0.9869	1	0.9984	0.9998
Std	0.1075	0.0409	0.0361	0.123	0.0533	0.0881	0.0937	0.0684	0.0215
Upper confidence limit	0.6402	0.8882	0.8834	0.4851	0.9543	0.7012	0.7341	0.8235	0.9281
Lower confidence limit	0.771	0.969	0.9593	0.6251	0.9464	0.8196	0.8562	0.9279	0.9866
Mean	0.7056	0.9286	0.9214	0.5551	0.9003	0.7604	0.7951	0.9757	0.9574

Fig. 10. Diagnosis results of VSPWM(4,6)

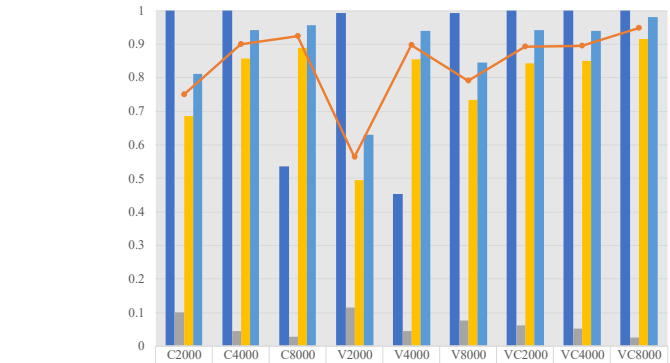

	C2000	C4000	C8000	V2000	V4000	V8000	VC2000	VC4000	VC8000
Final Accuracy	1	0.9993	0.5348	0.9933	0.454	0.993	1	1	1
Std	0.0995	0.0458	0.0288	0.1154	0.0458	0.0764	0.0614	0.0512	0.0261
Upper confidence limit	0.6864	0.8564	0.8893	0.4946	0.8551	0.7349	0.8428	0.8504	0.9156
Lower confidence limit	0.8122	0.9418	0.957	0.6302	0.9405	0.8453	0.9417	0.9407	0.9801
Mean	0.7493	0.8991	0.9231	0.5624	0.8978	0.7901	0.8922	0.8956	0.9478

Fig. 5. Diagnosis results of VSPWM(5,7)

In the experimental results diagrams, we comprehensively evaluated the diagnostic accuracy throughout the training process across various model structures. The figures respectively depict the final diagnostic accuracy, variance (std), upper bound of the confidence interval, next confidence interval, and mean diagnostic accuracy following 100 rounds of training.

We take the overall diagnostic mean value of each model training process as the primary measurement, as it effectively reflects both the diagnostic capability and convergence speed of the training process. As observed in the experimental results figures, when the diagnostic model employs only three-phase current data as input features, the mean diagnostic accuracy generally surpasses that achieved with only three-phase voltage data. Notably, when model structures remain constant, utilizing both three-phase voltage and current signals yields superior diagnostic results compared to using either signal in isolation.

Generally, when characteristic data is employed as the input data for the model, the diagnostic results obtained using the current data exhibit superior performance compared to those using voltage data. Furthermore, as the total amount of data increases after sampling, the model's performance demonstrates an upward trend. Nonetheless, due to the limited application of only one VSPWM at this juncture, an escalation in the input data size can impede the thorough extraction of features from the data. Consequently, this leads to feature redundancy and negatively impacts the model's overall performance.

From Fig. 12. to Fig. 14. illustrated the diagnostic outcomes when two VSPWMs are employed in VASPN. These figures further demonstrate that employing three-phase current as input features enhances the diagnostic accuracy of the model by using

three-phase voltage alone. Moreover, integrating both three-phase voltage and current signals concurrently consistently yields better results than using either signal independently.

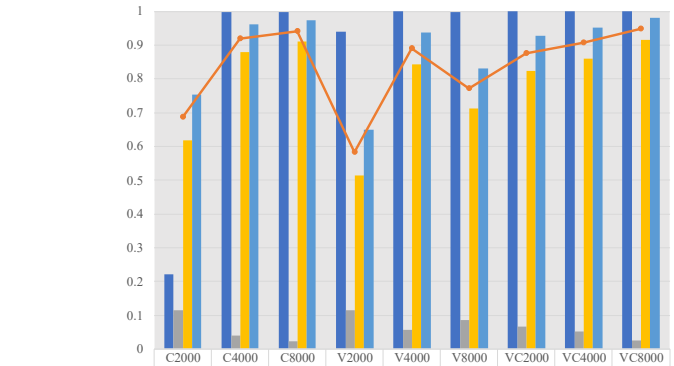

	C2000	C4000	C8000	V2000	V4000	V8000	VC2000	VC4000	VC8000
Final Accuracy	0.222	0.9971	0.997	0.9407	1	0.9988	1	1	1
Std	0.1152	0.0408	0.0237	0.1157	0.0575	0.0857	0.0663	0.0521	0.0261
Upper confidence limit	0.6185	0.88	0.9111	0.5147	0.8426	0.713	0.8237	0.8604	0.9156
Lower confidence limit	0.7539	0.9605	0.9725	0.6504	0.9384	0.8298	0.9264	0.9515	0.9801
Mean	0.6862	0.9203	0.9418	0.5826	0.8905	0.7714	0.8751	0.9059	0.9478

Fig. 6. Diagnosis results of VSPWM(3,5) (4,6)

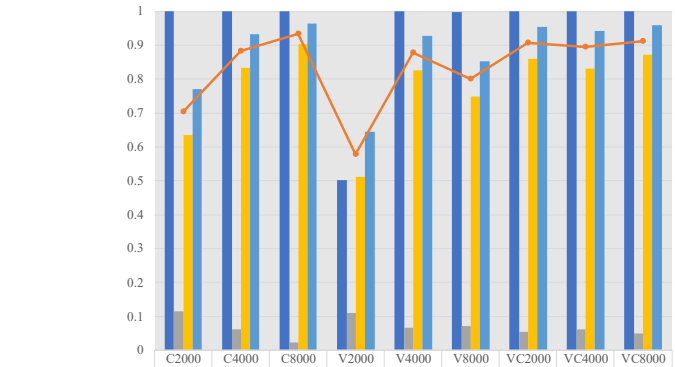

	C2000	C4000	C8000	V2000	V4000	V8000	VC2000	VC4000	VC8000
Final Accuracy	1	0.9993	0.9996	0.502	0.9993	0.9982	1	1	1
Std	0.116	0.0606	0.0239	0.1104	0.0669	0.071	0.0555	0.0612	0.0499
Upper confidence limit	0.6348	0.8335	0.9028	0.5108	0.8252	0.7475	0.8599	0.8309	0.8712
Lower confidence limit	0.7707	0.9317	0.9645	0.6434	0.9284	0.8538	0.954	0.9411	0.959
Mean	0.7027	0.8826	0.9337	0.5771	0.8768	0.8006	0.907	0.8957	0.9112

Fig. 7. Diagnosis results of VSPWM(3,5) (5,7)

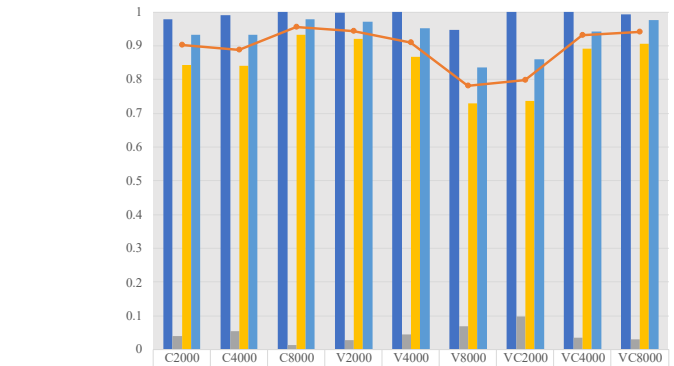

	C2000	C4000	C8000	V2000	V4000	V8000	VC2000	VC4000	VC8000
Final Accuracy	0.9791	0.9916	0.999	0.9971	1	0.9467	1	1	0.994
Std	0.0388	0.0535	0.0138	0.0288	0.0445	0.0684	0.0969	0.0357	0.0301
Upper confidence limit	0.8424	0.8412	0.932	0.9211	0.868	0.7302	0.7353	0.8912	0.9068
Lower confidence limit	0.9316	0.9335	0.979	0.971	0.9522	0.8346	0.8595	0.9431	0.9761
Mean	0.9026	0.8873	0.9555	0.9427	0.9101	0.7824	0.7974	0.9324	0.9415

Fig. 8. Diagnosis results of VSPWM(3,5) (5,7)

Similarly, when the input data type remains constant, the diagnostic performance of the model shows an upward trend with increasing data scale. At this point, when the parameters of VSPWM are set to (4,6) and (5,7), the overall performance of the model is noticeably inferior to that of the other two comparative models. However, the model utilizing VSPWM with parameters (3,5) demonstrates stable performance even with small-scale data under these conditions. Therefore, it is essential to further investigate the model performance when three different sets of VSPWM parameters are employed simultaneously.

Fig. 15. illustrates the use of VSPWM three times in VSPWN with respective parameters (3,5), (4,6), and (5,7). When both voltage and current data were employed simultaneously, VSPWN achieved diagnostic accuracies of 99.93%, 100%, and 100%, respectively. Throughout the entire training process, the average diagnostic accuracy of the corresponding model consistently outperformed other configurations. Therefore, the optimal final diagnostic model structure utilizes VSPWM three times within VSPWN, integrating both three-phase voltage and current data as primary feature inputs.

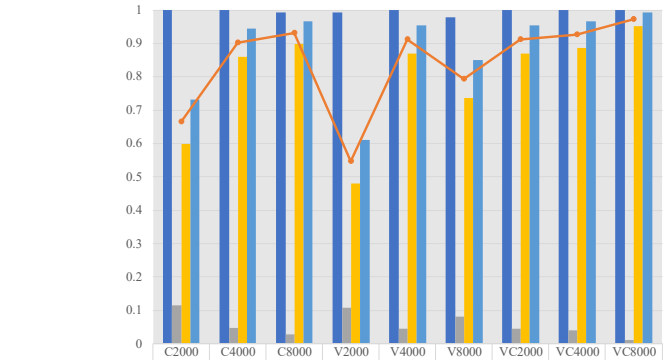

	C2000	C4000	C8000	V2000	V4000	V8000	VC2000	VC4000	VC8000
Final Accuracy	1	0.9998	0.994	0.994	0.9996	0.9775	0.9993	1	1
Std	0.1145	0.0464	0.0289	0.1071	0.0449	0.0799	0.045	0.0407	0.0105
Upper confidence limit	0.5977	0.8597	0.8981	0.4806	0.87	0.7375	0.8684	0.8853	0.9511
Lower confidence limit	0.7327	0.9456	0.966	0.6112	0.9545	0.8503	0.953	0.9657	0.9921
Mean	0.6652	0.9026	0.932	0.5459	0.9123	0.7939	0.9107	0.9255	0.9716

Fig. 9. Diagnosis results of VSPWM(3,5) (4,6) (5,7)

Moreover, to mitigate the influence of convolutional layer core counts and batch size on diagnostic accuracy during model training, we conducted comparative experiments across different channel configurations and batch sizes. Observationally, with consistent channel counts, the diagnostic accuracy of the model decreases as batch size increases. Conversely, when batch size remains constant, increasing the number of channels enhances diagnostic accuracy. Ultimately,

our findings indicate that the optimal configuration for peak performance of the diagnostic model occurs at Channel=64 and Batch_size=4

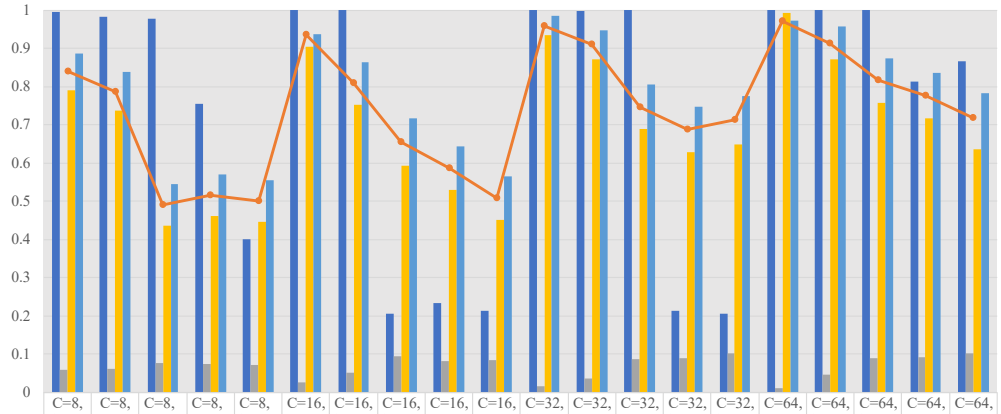

	C=8, bs=4	C=8, bs=8	C=8, bs=16	C=8, bs=32	C=8, bs=64	C=16, bs=4	C=16, bs=8	C=16, bs=16	C=16, bs=32	C=16, bs=64	C=32, bs=4	C=32, bs=8	C=32, bs=16	C=32, bs=32	C=32, bs=64	C=64, bs=4	C=64, bs=8	C=64, bs=16	C=64, bs=32	C=64, bs=64
Final Accuracy	0.9941	0.9818	0.9776	0.7541	0.4008	0.9996	0.9993	0.2048	0.2329	0.2129	0.9997	0.9977	0.9994	0.214	0.205	1	0.9997	1	0.8124	0.8654
Std	0.0586	0.0615	0.0755	0.0749	0.0723	0.0268	0.0504	0.0943	0.0813	0.0842	0.0163	0.037	0.0873	0.0894	0.1006	0.0105	0.0456	0.0881	0.0904	0.1028
Upper confidence limit	0.7904	0.7381	0.435	0.46	0.4464	0.904	0.7514	0.5933	0.5306	0.4497	0.9337	0.8712	0.6879	0.6278	0.6487	0.9921	0.8713	0.7563	0.7158	0.6356
Lower confidence limit	0.887	0.837	0.5446	0.5692	0.5538	0.9364	0.8646	0.7158	0.6444	0.5655	0.9847	0.948	0.8058	0.7471	0.7752	0.9716	0.9565	0.8748	0.8357	0.7815
Mean	0.8387	0.7875	0.4898	0.5146	0.5001	0.9367	0.808	0.6546	0.5875	0.5076	0.9592	0.9096	0.7468	0.6874	0.712	0.9716	0.9139	0.8156	0.7757	0.7175

Fig. 10. Effects of different channels and Batch_size on the model.

To visually demonstrate the feature extraction capabilities of VSPWM with varying parameters, t-SNE analysis was conducted on the diagnostic process of the mentioned model, as depicted in Fig. 17. It is evident that significant differences exist among the extracted features when employing VSPWM parameters (3,5), (4,6), and (5,7). However, upon their integration, the t-SNE plots align closely with the features extracted solely by VSPWM with parameters (5,7). Furthermore, the diagnostic accuracy of the model is higher when employing a three-layer VSPWM compared to a single-layer VSPWM, underscoring that VSPWM with diverse parameters effectively extracts varied feature information and mitigates the risk of overlooking less diverse features.

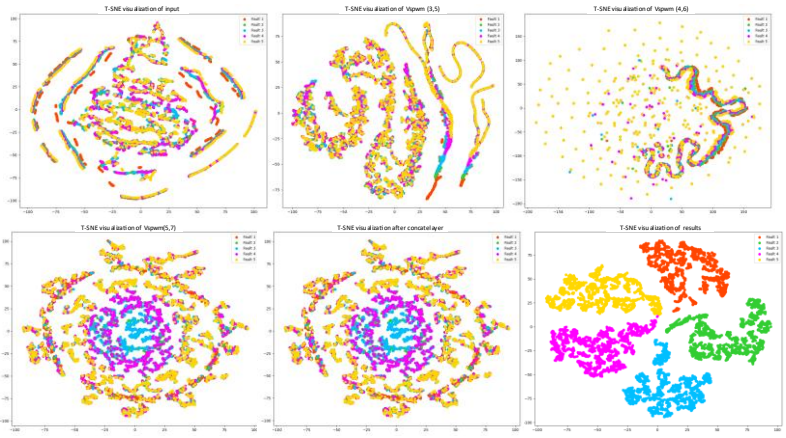

Fig. 11. The TSNE results of Feature.

5. Comparison With Other Methods

To demonstrate the effectiveness of the proposed method in this paper, diagnostic experiments were conducted on three-phase inverter PSF using various diagnostic models applied to original three-phase voltage and current signals. Additionally, to assess the noise resistance of the model, white Gaussian noise of varying magnitudes was added to the data to simulate real-world noise interference during data acquisition. The diagnostic results are presented in Fig 18.

To conduct comprehensive experimental verification, this paper selects several classical diagnostic models, including 1DCNN, 1DCNN-LSTM, and the Deep Residual Shrinkage Network (DRSN). Additionally, several novel optimized

diagnostic models are included, such as IWOA-1DCNN-LSTM[18], which leverages the improved Whale Optimization Algorithm to optimize the parameters of 1DCNN, and MTF-SPCNN[19], which diagnoses using two-dimensional feature images. The diagnostic accuracy of the HTISFF-VSPWN proposed in this paper is the highest under both raw data and noisy conditions, surpassing that of the DRSN model by 1.15%, 3.29%, and 0.37%, respectively. Notably, the proposed method requires only 60 seconds for each training round, which is 120 seconds less than the 180 seconds needed for the DRSN and 182 seconds less than that required for IWOA-1DCNN-LSTM. This efficiency can be attributed to the larger parameter values of the convolution layer in the IWOA-optimized 1DCNN, where an increase in the number of convolution kernels typically results in a longer diagnosis time. These findings underscore the superior performance of the proposed method.

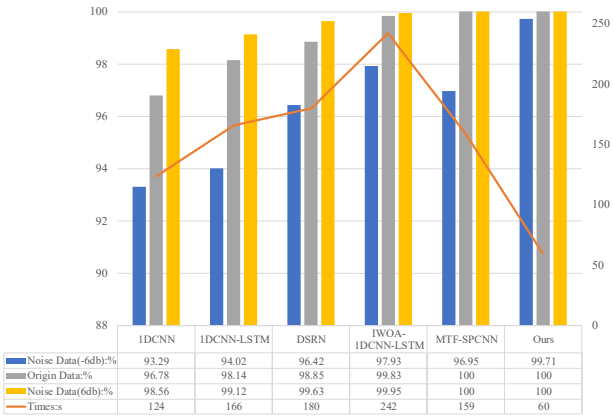

	1DCNN	1DCNN-LSTM	DSRN	IWOA-1DCNN-LSTM	MTF-SPCNN	Ours
Noise Data(-6db):%	93.29	94.02	96.42	97.93	96.95	99.71
Origin Data:%	96.78	98.14	98.85	99.83	100	100
Noise Data(6db):%	98.56	99.12	99.63	99.95	100	100
Times:s	124	166	180	242	159	60

Fig. 12. Results compared with other methods.

6. Conclusion

This paper proposes a diagnostic model, HTISFF-VSPWN, for parametric faults in three-phase inverters. The diagnostic model takes the three-phase voltage and current signals as input data. These signals undergo Hilbert transformation and subsequent sampling at regular intervals. The resulting transformed data are then combined to form the input features for the VSPWN diagnostic model. Upon input, these features undergo multi-scale convolution through two corresponding convolution layers to extract features of varying scales. Additionally, a reverse self-attention mechanism is employed to emphasize significant features while suppressing minor ones, thereby enabling effective extraction of distinguishing features between different degrees of PSF and enhancing diagnostic accuracy.

Comparative analysis with other methods demonstrates that the proposed model achieves superior diagnostic accuracy and robustness under noisy conditions. The proposed VSPWN enhances model diagnostic efficiency while preserving critical features through the collaboration of convolutional layers with varying lengths that operate asynchronously. Future research should prioritize the development of a universal diagnostic model adaptable to diverse operational conditions, thereby enhancing its generalizability. Furthermore, exploring adaptive structural adjustments within the model presents an important avenue for investigation.

References

1. Y. Luo, K. D. Li, C. Y. Chen *et al.,* "Model parameter identification-based inverter fault diagnosis method," *Journal of railway science and engineering.*, vol. 21 no. 5, pp. 2119-2130, May. 2024, doi: 10.19713/j.cnki.43-1423/u.T20231329.
2. J. Y. Jeong, S. Kwak, "Investigation of Loss Characteristics in SiC-MOSFET Based Three-Phase Converters Subject to Power Cycling and Short Circuit Aging," *Journal of Electrical Engineering & Technology*., vol. 18, no. 4, pp. 3049-3059, May. 2023, doi: 10.1007/s42835-023-01537-5.
3. M. Aydin, E. Beser, H. Kelebek, "Efficiency comparison of 2-level and 3-level Si IGBT based inverters," *2023 7th International Conference on Green Energy and Applications (ICGEA). Singapore, Singapore. IEEE.*, 2023, pp. 126-130, doi: 10.1109/ICGEA57077.2023.10125768.
4. B. Lu, S. K. Sharma, "A literature review of IGBT fault diagnostic and protection methods for power inverters," in *IEEE Transactions on Industry Applications*., vol. 45, no. 5, pp. 1770-1777, Sept.-oct. 2009, doi: 10.1109/TIA.2009.2027535.
5. Y. Y. Jiang, H. Cheng, J. Cui, *et al.,* "Soft fault diagnosis of photovoltaic inverter based on VMD wavelet energy," *Proceedings of the CSU-EPSA*., vol. 30, no. 11, pp. 19-25, 2018, doi: CNKI: SUN: DLZD.0.2018-11-004.
6. X. W. Wei, Y. G. Yang, Y. Zhang *et al.,* "Parallel Open-Circuit Fault Diagnosis Method for Cascaded Full-Bridge NPC Inverters with carrier phase shifted modulation," *Proceedings of the CSEE*., pp. 1-18, doi: 10.13334/j.0258-8013.pcsee.232447.

7. I. Jlassi, J. O. Estima, S. K. E. Khil *et al.,* "A Robust Observer-Based Method for IGBTs and Current Sensors Fault Diagnosis in Voltage-Source Inverters of PMSM Drives," in *IEEE Transactions on Industry Applications*., vol. 53, no. 3, pp. 2894-2905, May-June 2017, doi: 10.1109/TIA.2016.2616398.
8. B. Gou, Y. Xu, Y. Xia *et al.,* "An Online Data-Driven Method for Simultaneous Diagnosis of IGBT and Current Sensor Fault of Three-Phase PWM Inverter in Induction Motor Drives," in *IEEE Transactions on Power Electronics*., vol. 35, no. 12, pp. 13281-13294, Dec. 2020, doi: 10.1109/TPEL.2020.2994351.
9. Q. Y. Wang, W. P. Li, "Open-Circuit Fault Diagnosis Method for Traction Inverter Based on Average Voltage and Extreme Learning Machine," *China Railway Science*., vol. 44, no. 6, pp. 143-152, 2023.
10. Q. Sun, X. H. Yu, H. S Li *et al.,* "Adaptive feature extraction and fault diagnosis for three-phase inverter based on hybrid-CNN models under variable operating conditions," *Complex & Intelligent Systems*., vol. 8, no. 1, pp. 1-14, 2021, doi： 10.1007/S40747-021-00337-6.
11. B.Y. Song, Y.Y. Liu, J.Z.Fang, et al. An optimized CNN-BiLSTM network for bearing fault diagnosis under multiple working conditions with limited training samples, Neurocomputing, Vol.574, Jan. 2024. https://doi.org/10.1016/j.neucom.2024.127284
12. Q. Z. Zhao, Y. Li, S. M. Tian *et al.,* "Condition Monitoring and Fault Handling Method Based on Big Data Analysis of Intelligent Distribution Network," *Power System Technology.*, vol. 40, no. 3, pp. 774-780, 2016. doi: 10.13335/j.1000-3673.pst.2016.03.017.
13. B. Q. Qian, Q. Chen, Z. W. Zhang *et al.,* "Multi-task Transient Stability Assessment Based on Feature-level Fusion of Heterogeneous Data," *Automation of Electric power System.*, vol. 47, no. 9, pp. 118-128, 2023.
14. I. Bandyopadhyay, P. Purkait, C. Koley, "Performance of a Classifier Based on Time-Domain Features for Incipient Fault Detection in Inverter Drives," *in IEEE Transactions on Industrial Informatics.*, vol. 15, no. 1, pp. 3-14, Jan. 2019, doi: 10.1109/TII.2018.2854885.
15. Y. Y. Jiang, S. T. Zhang. "Research on soft fault diagnosis method of PV inverter based on improved VMD and CNN neural network," *Electrical measurement and instrumentation*., vol. 58, no. 2, pp. 158-163, 2021, doi: 10.19753/j.issn1001-1390.2021.02.025.
16. Z. Y. Li, Q. Chen, B. Q. Qian, *et al.,* "Health diagnosis of switch tube in grid-connected inverter based on Gramian angular field and parallel CNN," *Electric Power Automation Equipment*, pp. 1-11, Jul. 2024, doi: 10.16081/j.epae.202312032.
17. Y.B. Cui, R.J. Wang, Y.P. Si, *et al.,* "T-type inverter fault diagnosis based on GASF and improved AlexNet," Energy Reports, Vol.9, pp.2718-2731, Dec. 2023. https://doi.org/10.1016/j.egyr.2023.01.095
18. Y.Y. Jiang, L. Xia, J. Zhang, A fault feature extraction method for DC-DC Converters Based on Automatic Hyperparameter-Optimized 1-D Convolution and long short-term memory neural networks, IEEE Journal of emerging and selected topics in power electronics, Vol.10, no.4, Aug. 2022. https://doi.org/10.1109/JESTPE.2021.3131706
19. C.L. Lei, M.X. Jiao, S.Z. Ma, et al. Fault diagnosis method of small sample rolling bearing under variable working conditions based on MTF-SPCNN, Journal of Beijing university of aeronautics and astronautics, pp. 1-15.doi:10.13700/j.bh.1001-5965.2022.0927.